Volume 16
Number 9
7 March 2024
Pages 4336-4922

Nanoscale

rsc.li/nanoscale

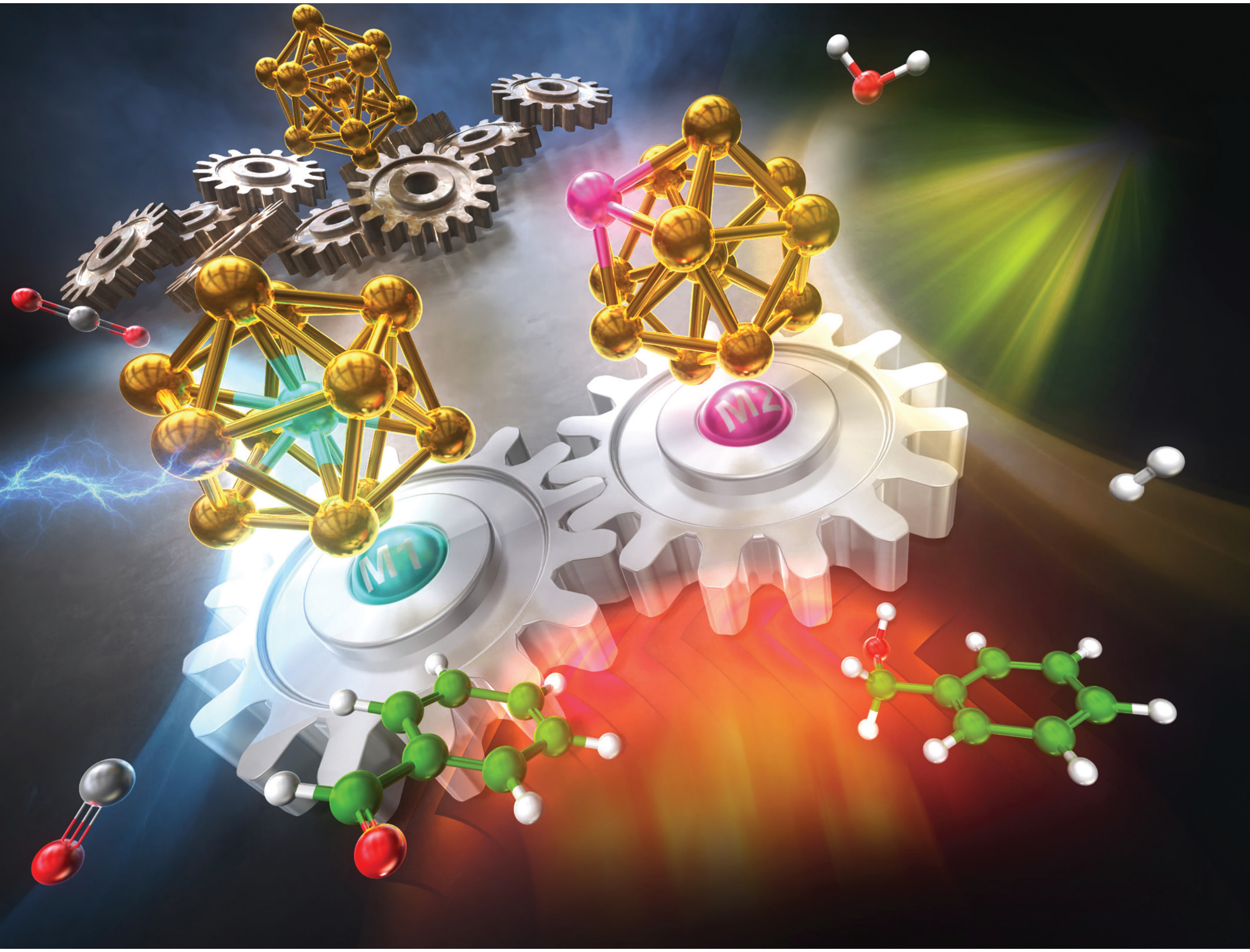

ISSN 2040-3372

MINIREVIEW
Tatsuya Tsukuda *et al.*
Atomically precise Au and Ag nanoclusters doped with a single atom as model alloy catalysts

Nanoscale

ROYAL SOCIETY OF CHEMISTRY

MINIREVIEW

View Article Online
View Journal | View Issue

Cite this: *Nanoscale*, 2024, **16**, 4514

Atomically precise Au and Ag nanoclusters doped with a single atom as model alloy catalysts

Shinya Masuda, Kosuke Sakamoto and Tatsuya Tsukuda *

Received 27th November 2023,
Accepted 27th December 2023

DOI: 10.1039/d3nr05857c

rsc.li/nanoscale

Gold and silver nanoclusters (NCs) composed of <200 atoms are novel catalysts because their catalytic properties differ significantly from those of the corresponding bulk surface and can be dramatically tuned by the size (number of atoms). Doping with other metals is a promising approach for improving the catalytic performance of Au and Ag NCs. However, elucidation of the origin of the doping effects and optimization of the catalytic performance are hampered by the technical challenge of controlling the number and location of the dopants. In this regard, atomically precise Au or Ag (Au/Ag) NCs protected by ligands or polymers have recently emerged as an ideal platform because they allow regioselective substitution of single Au/Ag constituent atoms while retaining the size and morphology of the NC. Heterogeneous Au/Ag NC catalysts doped with a single atom can also be prepared by controlled calcination of ligand-protected NCs on solid supports. Comparison of thermal catalysis, electrocatalysis, and photocatalysis between the single-atom-doped and undoped Au/Ag NCs has revealed that the single-atom doping effect can be attributed to an electronic or geometric origin, depending on the dopant element and position. This minireview summarizes the recent progress of the synthesis and catalytic application of single-atom-doped, atomically precise Au/Ag NC catalysts and provides future prospects for the rational development of active and selective metal NC catalysts.

1 Introduction

Metal nanoclusters (NCs), composed of <200 metal atoms, are promising catalytic materials because they exhibit novel and size-specific chemical reactivities that are significantly different from those of metal nanoparticles larger than a few nanometers.[1–5] Alloying is a straightforward and effective way to further improve their catalytic performance, which is mainly tuned by geometric (or ensemble) and/or electronic (or ligand) effects.[6–11] However, the reason for the improved catalytic activity by alloying is not easily explained due to the polydisperse nature of the structural parameters of conventional alloy NCs, such as the size (total number of atoms), composition, and mixing mode (*e.g.*, solid solution, core–shell, and segregated structures). To overcome this situation, it is necessary to precisely control these key parameters without changing other parameters.

Single-metal-atom doping is the first, but significant, step toward the optimization of the catalysis of a metal NC, given that it is composed of a countable number of atoms and has a surface-rich structure. Single-atom doping reduces the numerous factors to be controlled in the conventional mixing modes only to control the dopant position. Single-atom-doped (SAD) metal NCs not only lead to understanding the origin of the doping effects on catalysis, but also provide a design principle for alloy catalysts. Nevertheless, it is not a trivial matter to regioselectively dope a single atom without changing the size and structure of the base metal NCs.

Such synthetic problems can be solved by using atomically precise gold or silver (Au/Ag) NCs protected by organic ligands,[12–33] the structures of which are determined by single-crystal X-ray diffraction (SCXRD) analysis. For example, single atoms of various transition metals have been regioselectively introduced to an icosahedral Au_{13} NC while retaining the structure.[17,19,23,24] In addition, recent systematic studies have revealed how the energies of the highest-occupied and lowest-unoccupied molecular orbitals (HOMO and LUMO, respectively) are modulated upon doping and how the relaxation dynamics of the electronically excited state are affected by doping. Thus, the SAD Au/Ag NCs and their undoped counterparts (Scheme 1) protected by ligands are ideal platforms for elucidating the doping effects, especially on electrocatalysis and photocatalysis, which are promoted by the electron transfer between reactants through the ligand layer.

On the other hand, for studying the doping effects on thermal catalysis, the SAD NC should be stabilized while exposing a part of the surface. This requirement is met by stabilizing the SAD NC with a polymer or by immobilizing the

---

Department of Chemistry, Graduate School of Science, The University of Tokyo, 7-3-1 Hongo, Bunkyo-ku, Tokyo 113-0033, Japan. E-mail: tsukuda@chem.s.u-tokyo.ac.jp

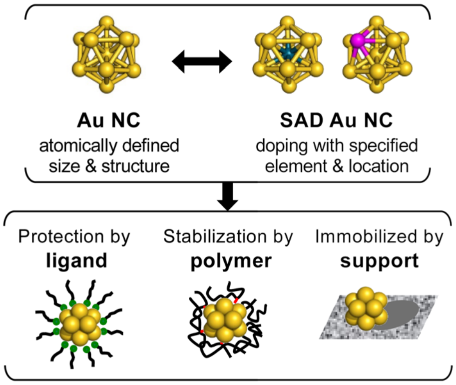

Scheme 1 Pure *vs.* single-atom-doped (SAD) Au NC.

SAD NC on a solid support (Scheme 1). The dopant located inside the SAD NC modulates the electronic structure of the reaction site on the surface, while the dopant on the surface may directly act as a reaction site for catalytic conversion. The latter type can be viewed as single-atom alloy catalysts[34–38] supported by a defined number of base metal atoms. However, achieving atomically precise synthesis and structure determination of these types of SAD NCs is still very difficult.

This minireview surveys the research in the emerging area of the single-atom-doping effects on the catalysis of atomically precise Au/Ag NCs. The catalysts include SAD Au/Ag NCs protected by organic ligands, sparsely coated by polymers, and immobilized on solid supports (Scheme 1). Section 2 describes the atomically precise syntheses and structures of the SAD Au/Ag NCs. The doping effects on the thermal catalysis, electrocatalysis, and photocatalysis are respectively introduced in sections 3–5. Section 6 summarizes the roles of each dopant in various types of catalysis and presents the future prospects for the rational development of active and selective metal NC catalysts.

2 Synthesis and structural characterization

This section presents an overview of the syntheses and structures of three types of SAD Au/Ag NCs as well as the corresponding pure Au/Ag NCs treated in this review (Tables 1–3).[39–63] The atomic packing structures and the dopant locations were determined by a combination of methods, including SCXRD,[57,58,61,63–69] nuclear magnetic resonance (NMR) spectroscopy,[40,70] X-ray absorption fine structure (XAFS) spectroscopy.[39,44,45,60,71,72] high-resolution transmission electron microscopy (HRTEM),[59,73,74] and density functional theory (DFT) calculations.[40,60,75,76]

2.1 Ligand-protected single-atom-doped Au/Ag nanoclusters

Ligand-protected monometallic Au/Ag NCs with crystallographically determined structures serve as ideal references for studying the doping effects on catalysis.[77–89] Atomically precise syntheses of the ligand-protected Au/Ag NCs were achieved by rigorous isolation and fractionation from relatively monodisperse Au/Ag NCs.[12,13,22,25] Many examples of ligand-protected Au/Ag NCs have been reported for decades.[12–33] The stability of Au/Ag NCs is governed by electronic structures: spherical Au/Ag NCs gain high stability when the total number of valence electrons matches specific numbers such as 2, 8, 18, 20, 34, and so on.[90–92] For example, the thiolate (SR)-protected Au NC $[Au_{25}(SR)_{18}]^-$ with an icosahedral Au_{13} core takes a closed electron configuration $(1S)^2(1P)$,[25] where 1S, 1P, 1D, 2S, 1F, 2P, and so on are molecular orbitals that are distributed over the Au_{13} core and accommodate the valence electrons. These Au/Ag NCs are viewed as chemically modified Au/Ag superatoms because their hierarchical electronic structures are similar to the conventional atomic orbitals. Table 1 lists the SAD Au/Ag NCs introduced in this minireview: those protected by phosphines (entries 1–3), thiolates (entries 4–7 and 9–13), and alkynyls (entries 8 and 14).

The following text introduces four synthetic approaches to doping a single atom to ligand-protected Au/Ag NCs. The most common one is the co-reduction of ions of the base metal (Au/Ag) and dopant M in the presence of ligands (Scheme 2a). This approach is effective for doping transition metals of groups 9 and 10 (Pt, Pd, Ir, Rh, *etc.*). Simultaneous reduction produces not only SAD NCs, but also undoped NCs, thereby requiring further purification. For example, Negishi *et al.* isolated $PdAu_{24}(SC12)_{18}$ (SC12 = $SC_{12}H_{25}$) *via* reverse-phase high-performance liquid chromatography.[75] Jin *et al.* employed selective decomposition of undoped $Au_{25}(SR)_{18}$ with hydrogen peroxide (H_2O_2) to isolate $PtAu_{24}(SR)_{18}$.[40] Most of the ligand-protected SAD Au/Ag NCs were synthesized by co-reduction (entries 1–5, 10, 11, 13 and 14, Table 1).[39,40,42,43,46–52,54,55,58,60–63,93]

Galvanic replacement of metal elements driven by a redox reaction is a well-known phenomenon in the bulk surface. It is, for example, used in the synthesis of $AuAg_{24}(SR)_{18}$ by mixing $Ag_{25}(SR)_{18}$ and $Au(PPh_3)Cl$ (entry 9, Table 1), where Ag^0 is oxidized and then dissolved in solution, while Au^+ is reduced and deposited on the NC (Scheme 2b).[46,57,62] On the other hand, $MAu_{24}(SR)_{18}$ (M = Cd or Hg) was synthesized by mixing $Au_{25}(SR)_{18}$ with $M(NO_3)_2$ (entries 6 and 7, Table 1).[41,53] This process is called anti-galvanic replacement and is specific to small metal NCs, where the most electronegative Au is dissolved as Au^+ in solution (Scheme 2c). A group 12 element is usually introduced into pure Au NCs *via* an anti-galvanic replacement reaction.

SAD NCs can also be obtained *via* the growth reaction of pure and doped Au NCs as the seed (Scheme 2d). $MAu_8(PPh_3)_8$ (M = Pd or Pt) was converted to $HMAu_8(PPh_3)_8$ with eight electrons by doping with hydride (H^-).[94] This hydride-doped NC was transformed by reacting with metal complexes to a variety of NCs including $MAu_{24}(SR)_{18}$, $MAu_{24}(C{\equiv}CAr^F)_{18}$, and $MAu_{12}(dppe)_5Cl_2$ (M = Pd or Pt) (entries 3, 8 and 13, Table 1).[56,58,69] The SAD NCs can be synthesized on a large scale (~100 mg) by taking advantage of the scalability of the $MAu_8(PPh_3)_8$ precursors and the efficient transformation.

Table 1 List of single-atom-doped Au/Ag nanoclusters protected by ligands and catalytic reactions for the elucidation of doping effects

	Formula and geometric structure						
Entry	Undoped NC	Doped NC	M	Synthesis method	Support	Catalytic reactions	Ref.
1[a]	$Au_9(PPh_3)_8$ 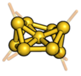	$MAu_8(PPh_3)_8$ 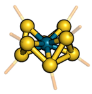	Pd	Coreduction	–	Oxidation of alcohols Reduction of 4-nitrobenzene	50
					Montmorillonite	CO_2 Hydrogenation	54
2[a]	$Au_{11}(PPh_3)_7Cl_2$[b] 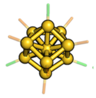	$MAu_{11}(PPh_3)_7Cl_2$ 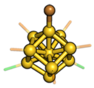	Cu	Coreduction	CeO_2	Glaser coupling	63
3[c]	$Au_{13}(dppe)_5Cl_2$ 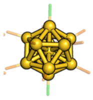	$MAu_{12}(dppe)_5Cl_2$ 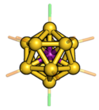	Pd, Pt, Rh, Ir	Coreduction, cluster conversion	–	Photoredox cycloaddition of bisenone	58
4	$Au_{25}(SR)_{18}$ 	$MAu_{24}(SR)_{18}$ 	Pd	Coreduction	C/GCE[d]	Electrocatalytic HER, OER, ORR	52[e]
					C/GDL[f]	CO_2 electroreduction	51[e]
5			Pt	Coreduction	TiO_2	Styrene oxidation	40[e]
					C/GDL[f]	Electrocatalytic HER	42[g], 47[g], and 55[g]
					MCNT[h]	Formic acid electrooxidation	48[i]
6			Hg	Anti-galvanic replacement	–	Reduction of 4-nitrobenzene	41[e]
7			Cd	Anti-galvanic replacement	Carbon paper	CO_2 electroreduction	53[e]
8[j]	$Au_{25}(C\equiv CAr^F)_{18}$ 	$MAu_{24}(C\equiv CAr^F)_{18}$ 	Pt	Cluster conversion	C/GCE[d]	Electrocatalytic HER	56
9[k]	$Ag_{25}(SPhMe_2)_{18}$ 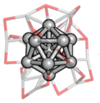	$MAg_{24}(SPhMe_2)_{18}$ 	Au	Galvanic replacement	–	Carboxylation of terminal alkynes	46
					TiO_2	Photocatalytic HER	62
10[k]			Pd	Coreduction	–	Carboxylation of terminal alkynes	46
					TiO_2	Photocatalytic HER	62
11[k]			Pt	Coreduction	–	Carboxylation of terminal alkynes	46
					$g\text{-}C_3N_4$[l], TiO_2	Photocatalytic HER	43 and 62
12[k]			Ni	Anti-galvanic replacement	C/GCE[d]	Electrocatalytic HER	57
13[m]	$Au_{38}(SCH_2Ph^tBu)_{24}$ 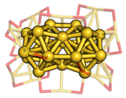	$MM'Au_{36}(SCH_2Ph^tBu)_{24}$ 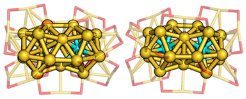	Pt	Coreduction, cluster conversion	Carbon paper	CO_2 electroreduction	60
14[n]	$Au_{43}(C\equiv C^tBu)_{20}$ 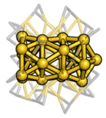	$MAu_{42}(C\equiv C^tBu)_{20}$ 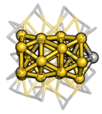	Ag	Coreduction	Al_2O_3	Oxidation of alcohols	61

[a] PPh_3: triphenylphosphine. [b] Undoped Au cluster: $Au_{11}(PPh_3)_7Cl_3$. [c] dppe: 1,2-bis(diphenylphosphino)ethane. [d] GCE: glassy carbon electrode. [e] SR = PET: 2-phenylethanethiolate. [f] GDL: gas diffusion layer. [g] SR = SC6: hexanethiolate. [h] MCNT: multi-wall carbon nanotube. [i] SR = SC12: dodecanethiolate. [j] $HC\equiv CAr^F$: 3,5-bis(trifluoromethyl)ethynylbenzene. [k] $SPhMe_2$: 2,4-dimethylbenzenethiolate. [l] $g\text{-}C_3N_4$: graphitic carbon nitride. [m] $HSCH_2Ph^tBu$: 4-*tert*-butylbenzyl mercaptan. [n] $HC\equiv C^tBu$: 3,3-dimethyl-1-butyne. Color code: yellow, Au; turquoise, Pd; brown, Cu; purple, Rh; cyan, Pt; pink, Cd; silver, Ag. Protection motifs are in the line-view; orange, P; light green, Cl; red, S; gray, C. Organic moieties of ligands and hydrogen atoms are omitted for clarity.

Table 2 List of single-atom-doped Au nanoclusters stabilized by PVP and catalytic reactions for the elucidation of doping effects

	Formula[a] and proposed geometric structure[b]				
Entry	Undoped Au NC	Doped NC	Synthesis method	Catalytic reactions	Ref.
1	Au_{24}:PVP 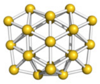	$PdAu_{23}$:PVP 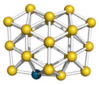	Coreduction	Oxidation of alcohols Hydrogenation of alkynes and alkenes	59 59
2	Au_{34}:PVP 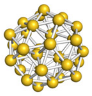	$PdAu_{33}$:PVP 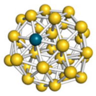	Coreduction	Oxidation of alcohols Hydrogenation of olefins	44 44 and 45
3		$RhAu_{34}$:PVP 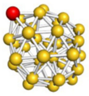	Coreduction	Hydrogenation of olefins	45

[a] PVP: polyvinylpyrrolidone. [b] DFT-optimized structure. Color code: yellow, Au; turquoise, Pd; and red, Rh.

Table 3 List of single-atom-doped Au/Ag nanoclusters immobilized on a solid support and catalytic reactions for the elucidation of doping effects

Entry	Formula and dopant location	Precursor and calcination conditions	Catalytic reactions	Ref.
1	$PdAu_{24}$/CNT[a] 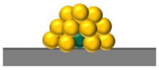 Interface	$PdAu_{24}(SC12)_{18}$[b], 450 °C, 2 h in a vacuum	Oxidation of alcohols	39
2	$PtAg_{24}$/g-C_3N_4[c] 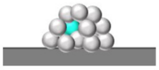 Inside	$PtAg_{24}(SPhMe_2)_{18}$[d], 150 °C, 2 h under Ar	Photocatalytic HER	43
3	$PdAu_{24}/BaLa_4Ti_4O_{15}$ 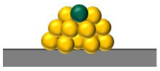 Surface	$PdAu_{24}(PET)_{18-y}(p\mathrm{MBA})_y$[e,f], 300 °C, 80 min in a vacuum	Water splitting	49
4	$PtAu_{24}/BaLa_4Ti_4O_{15}$ 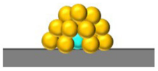 Interface	$PtAu_{24}(PET)_{18-y}(p\mathrm{MBA})_y$[e,f], 300 °C, 80 min in a vacuum	Water splitting	49

[a] CNT: carbon nanotube. [b] SC12: dodecanethiolate. [c] g-C_3N_4: graphitic carbon nitride. [d] $SPhMe_2$: 2,4-dimethylbenzenethiolate. [e] PET: 2-phenylethanethiolate. [f] *p*MBA: *p*-mercaptobenzoic acid. Color code: yellow, Au; gray, Ag; turquoise, Pd; and cyan, Pt.

The structures determined by SCXRD and other methods listed in Table 1 suggest that the location of the dopants depends on the element group. Element M of groups 9 and 10 (Ir, Rh, Pt and Pd) is located at the center of the crown-shaped $M@Au_8$ protected by phosphine (entry 1, Table 1) and the icosahedral $M@Au_{12}$/$M@Ag_{12}$ protected by phosphine, thiolate, or alkynyl (entries 3–5 and 8–13, Table 1). The $M@Au_{12}$ cores become more compact and symmetrical by doping with element M positioned at the lower left of the periodic table due to the reduction of the atomic radius of M. In contrast, element M of groups 11 and 12 (Au, Ag, Cu, Hg and Cd) is attached on the surface of $Au@Au_{10}$ protected by phosphine (entry 2, Table 1) and incorporated into the surface of the icosahedral $Au@MAu_{11}$ protected by thiolate (entries 6 and 7, Table 1) and $Au_{12}@Au_{20}$ protected by alkynyl (entry 14, Table 1). Electrochemical measurements and optical absorption spectroscopy on $M@Au_{12}$ revealed that the HOMO is energetically upshifted and the HOMO–LUMO gap is expanded by doping with element M positioned at the lower left of the periodic table. The former trend can be understood by a two-step jellium model (Fig. 1): the central part of the jellium potential of the $M@(Au^+)_{12}$ ($M = Au^+, Pt^0, Ir^-$) superatomic core becomes shallower by replacing Au^+ with Pt^0 and even shallower with Ir^-. The lifetime of the electronically excited state becomes elongated up to the μs range by doping with M positioned at the lower left of the periodic table, such as Pt and Ir (energy gap law).[95] The ligand layer acts as a "catalytic poison" for thermal reactions, while ligand-protected SAD Au/Ag NCs act as electrocatalysts by forming active sites through partial removal of the ligand,[96–101] and as photocatalysts by electron transfer through the ligand layer.

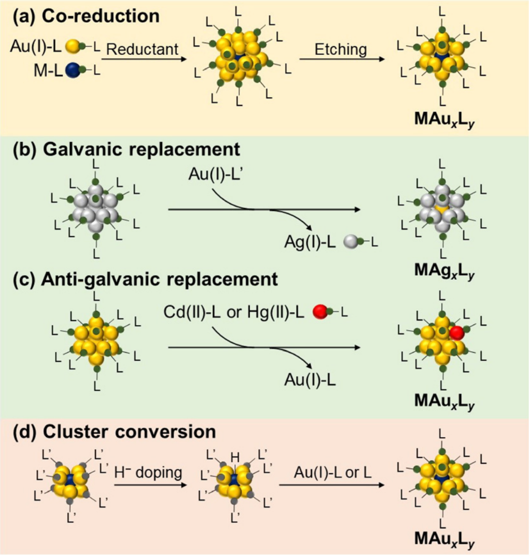

Scheme 2 Representative synthetic methods of SAD Au/Ag NCs protected by organic ligands.

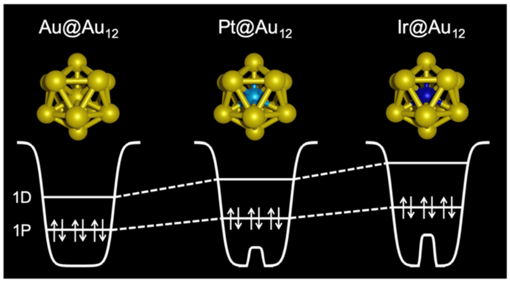

Fig. 1 Schematic illustration of the two-step jellium potential and superatomic orbitals of $M@(Au^+)_{12}$ ($M = Au^+, Pt^0, Ir^-$). Reproduced from ref. 95 with permission from the American Chemical Society, Copyright 2020.

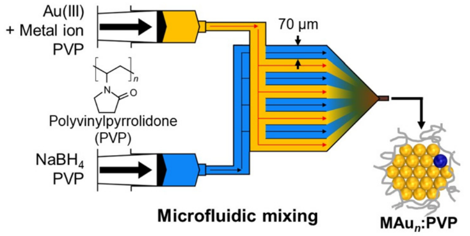

Scheme 3 Schematic of the synthetic method of SAD Au NCs stabilized by PVP.

2.2 Polyvinylpyrrolidone-stabilized single-atom-doped Au nanoclusters

For catalytic application for thermal reactions, NCs should be stabilized by polymers while exposing part of the surface.[102,103] Atomically precise synthesis of Au_n NCs (n = 24, 34, 38) was recently achieved using polyvinylpyrrolidone (PVP) as a stabilizer.[59,73,74] The key factors to this success were: (1) kinetic control of the cluster formation by homogeneous and rapid mixing of Au ions and a strong reducing agent in the presence of an excess amount of PVP (Scheme 3), and (2) application of matrix-assisted laser desorption/ionization mass spectrometry (MALDI-MS) for evaluating the cluster size n and the purities of Au_n NCs.[44,45,59] This approach has been applied for PVP-stabilized SAD Au NCs: $PdAu_{23}$:PVP,[59] $PdAu_{33}$:PVP,[44] or $RhAu_{34}$:PVP[45] was obtained by the co-reduction of Au ions and a controlled amount of Pd or Rh precursors in the microfluidic mixer (entries 1–3, Table 2). The geometric structures of Au_{24}:PVP and $Au_{23}Pd_1$:PVP were characterized by DFT calculations, aberration-corrected TEM (ACTEM), extended XAFS (EXAFS) analysis, and Fourier transform infrared (FT-IR) spectroscopy of the adsorbed CO. These results showed that $Au_{23}Pd_1$:PVP takes polydisperse structures with all the constituent atoms including the Pd atom on the surface, but all the optimized structures of $Au_{23}Pd_1$:PVP have the same atomic arrangements as the undoped Au_{24}:PVP (entry 1, Table 2).[59] Rh–K and Pd–K edge XAFS analysis on $PdAu_{33}$:PVP[44] and $RhAu_{34}$:PVP[45] revealed that Pd is incorporated into the surface of the Au_{33} NC (entry 2, Table 2), while the Rh atom is attached to the surface of the Au_{34} NC (entry 3, Table 2).

2.3 Solid-supported single-atom-doped Au/Ag nanoclusters

Ligand-protected SAD Au/Ag NCs adsorbed on solid materials in the intact form can be used as catalysts for electrocatalytic and photocatalytic reactions. In contrast, naked SAD Au/Ag NCs immobilized on solid supports exhibit a wider scope of applicability than ligated NCs as the reactants can be activated by direct interaction with the NC surface. However, naked SAD Au/Ag NCs cannot be synthesized with atomic precision on supports by conventional methods, such as impregnation and deposition–precipitation. An alternative synthetic strategy is to remove the ligands from the well-defined SAD Au/Ag NCs on solid supports (Scheme 4).[81] Ligand removal was conducted by thermal treatment, H_2O_2 treatment, or $NaBH_4$ reduction.[82,104] The intrinsic challenge is to avoid sintering of the NCs during the ligand removal. This problem was solved by reducing the density of the NCs on the supports by lowering the loading or using supports with a large specific surface area. Suppression of NC aggregation was confirmed by ACTEM and EXAFS. The inherent drawback of the approach shown in Scheme 4 is that

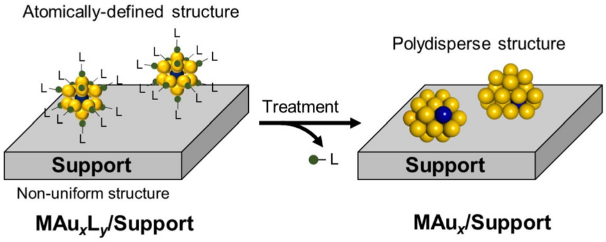

Scheme 4 Schematic of the synthetic method of SAD Au NCs on a solid support.

the geometric structures of the resulting NCs are not uniform due to the stochastic nature of the ligand desorption process and the non-uniform surface structures of the supports. Nonetheless, EXAFS provides key structural information on whether the dopant is exposed on the NC surface or confined within the NC based on the coordination number of the M–Au (Ag) bonds. The corresponding heterogeneous catalysts together with the dopant positions are listed in Table 3. The position of the dopant seems to be determined by the strength of its bonding to the surrounding Au/Ag atoms and to the solid support. For example, Pd in a $PdAu_{24}$/carbon nanotube (CNT) is located at the interface with CNT (entry 1, Table 3), but is on the surface when $PdAu_{24}$ is deposited on $BaLa_4Ti_4O_{15}$ (entry 3, Table 3). Barrabés *et al.* observed by *operando* diffuse reflectance infrared Fourier transform spectroscopy that the heating of $PdAu_{24}(SR)_{18}$ at 250 °C under an O_2 atmosphere followed by using H_2 led to the migration of the Pd atom from the center of the core to the surface.[93]

3 Thermal catalysis

3.1 Oxidation reactions

Zhu *et al.* compared the catalytic activity of $[PdAu_8(PPh_3)_8]^{2+}$ and its undoped counterpart $[Au_9(PPh_3)_8]^{3+}$ (entry 1, Table 1) for benzyl alcohol (BnOH) oxidation (eqn (1)).[50]

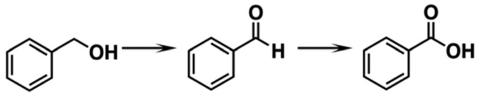

(1)

$[PdAu_8(PPh_3)_8]^{2+}$ showed catalytic activity and high selectivity to benzaldehyde, while $[Au_9(PPh_3)_8]^{3+}$ did not. The preservation of $[PdAu_8(PPh_3)_8]^{2+}$ under catalytic conditions was confirmed by ultraviolet-visible (UV-Vis) absorption spectroscopy, TEM, and FT-IR. This result suggested that the exposed Pd site was a reaction site. Mechanistic studies by electron paramagnetic resonance (EPR) spectroscopy showed that the superoxide species was formed only on $[PdAu_8(PPh_3)_8]^{2+}$. The partial density of states (PDOS) obtained by DFT calculations implied that O_2 was more strongly adsorbed to the central Pd dopant of $[PdAu_8(PPh_3)_8]^{2+}$ than to the central Au of $[Au_9(PPh_3)_8]^{3+}$. This difference resulted in the preferential formation of the superoxide species by $[PdAu_8(PPh_3)_8]^{2+}$ for BnOH activation.

Mason *et al.* recently compared the catalytic activity between $AgAu_{42}(C{\equiv}C^tBu)_{20}$ having an exposed Ag site on the surface and $AuAu_{42}(C{\equiv}C^tBu)_{20}$ (entry 14, Table 1) for BnOH oxidation (eqn (1)) using *tert*-butyl hydroperoxide (TBHP) as an oxidant.[61] The conversion decreased from 52% to 18% upon Ag doping. UV-Vis absorption spectroscopy and scanning TEM (STEM) supported the retention of the original cluster during catalysis. Topographic steric hindrance maps indicated that the Ag atom of $AgAu_{42}(C{\equiv}C^tBu)_{20}$ was geometrically more buried in the core than the Au atom at the corresponding position in $Au_{43}(C{\equiv}C^tBu)_{20}$, resulting in poorer accessibility of the reactants. The negative doping effect of Ag was also ascribed to the lower ability of the Ag site to abstract hydride from the alkoxide compared to the ability of the Au site.

Jin *et al.* reported that $Au_{25}(PET)_{18}/TiO_2$ and $PtAu_{24}(PET)_{18}/TiO_2$ exhibited 58.9% and 90.8% conversion in styrene oxidation, respectively, using iodobenzene diacetate ($PhI(OAc)_2$) as an oxidant (eqn (2)).[40]

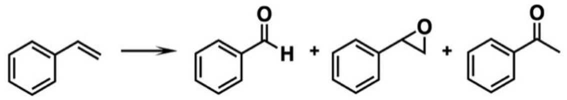

(2)

Since the Pt dopant of $PtAu_{24}(PET)_{18}$ located at the center of the Pt@Au_{12} core (entry 5, Table 1) cannot serve as a reaction site, modulation of the electronic structure plays a crucial role in promoting catalysis.

Tsukuda *et al.* found the enhancement of the alcohol oxidation catalysis of PVP-stabilized colloidal Au_{24} NCs by using a Pd dopant (entry 1, Table 2).[59] $PdAu_{23}$:PVP and Au_{24}:PVP exhibited pseudo-first-order reaction rate constants of 2.3 and 0.87 h^{-1}, respectively, in the aerobic oxidation of BnOH (eqn (1)). UV-Vis absorption spectroscopy and MALDI-MS spectrometry revealed that these clusters are preserved after catalysis. The enhancement was also observed for other *para*-substituted benzyl alcohols. DFT calculations predicted that hydride adsorbs more strongly on the Pd atom on the surface of $PdAu_{23}$ than on the Au atom of Au_{24}. Given that the rate-determining step (RDS) of eqn (1) was hydride abstraction from the α-carbon of benzyl alkoxide, the surface Pd atom acted as an efficient adsorption site for hydride, resulting in an enhanced activity (Fig. 2).

Tsukuda *et al.* reported the effect of single-atom doping on BnOH oxidation (eqn (1)) by using $PdAu_{24}$/CNT and Au_{25}/CNT (entry 1, Table 3).[39] The conversions by $PdAu_{24}$/CNT and Au_{25}/CNT were 74% and 22%, respectively, indicating that the catalytic activity was significantly enhanced upon Pd atom doping. TEM images after catalysis showed the same average particle size as with the fresh sample, suggesting that the cluster was not aggregated. Given that the Pd dopant atom was buried in the Au NC and located at the interface with the CNT support,[71,76] the enhanced catalytic activity was explained by the formation of the anionic Au surface *via* the electron transfer from Pd to Au, which facilitated the activation of O_2 more effectively. Namely, the role of the Pd atom differs from that proposed for $PdAu_{23}$:PVP.

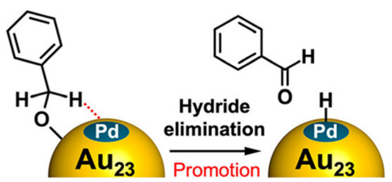

Fig. 2 Schematic illustration of the proposed mechanism by Pd doping on Au_{24}:PVP. Reproduced from ref. 59 with permission from the American Chemical Society, Copyright 2022.

3.2 Reduction reactions

Wu *et al.* observed that $HgAu_{24}(PET)_{18}$ (entry 6, Table 1) showed higher activity than $Au_{25}(PET)_{18}$ for the reduction of 4-nitrobenzene using $NaBH_4$ as a reductant (eqn (3)).[41] The cluster was preserved based on the results of UV-Vis absorption spectroscopy and MALDI-MS spectrometry.

(3)

Tsukuda compared the catalytic activity of $PdAu_{33}$:PVP and $RhAu_{34}$:PVP (entries 2 and 3, Table 2) with respect to undoped Au_{34}:PVP for the hydrogenation of olefins using H_2 as a reductant (eqn (4)).[44,45]

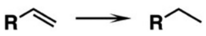

(4)

$RhAu_{34}$:PVP showed remarkably higher activity in the hydrogenation of olefins compared to that of Au_{33}:PVP, while $PdAu_{33}$:PVP showed moderate activity. Both Rh and Pd served as reaction sites for H_2 activation, while the higher activity of $RhAu_{34}$:PVP was ascribed to the lower coordination state of the Rh atom.

3.3 CO_2 fixation reactions

Zhu *et al.* compared the catalytic properties of $MAg_{24}(SPhMe_2)_{18}$ (M = Ag, Au, Pd, Pt) (entries 9–11, Table 1) for carboxylation of various terminal alkynes (R–C≡C–H; R = Ph, *p*MePh, *m*MePh, *p*NH_2Ph, *p*ClPh, *p*CHOPh) into the corresponding propiolic acids (eqn (5)).[46]

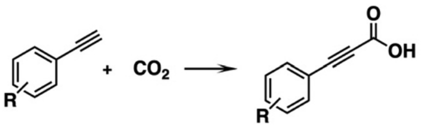

(5)

The catalytic activity was enhanced in the order of M = Ag < Pd ≈ Pt < Au. Furthermore, the catalysts could be reused without a significant loss of activity for M = Au, Pd, and Pt, while the undoped NCs (M = Ag) decomposed after the catalytic usage. This result demonstrated that the dopant atom enhanced not only the activity but also the stability of the NCs. UV-Vis absorption spectra of spent clusters showed no drastic change after catalytic cycles.

Zhu *et al.* intercalated $[Au_9(PPh_3)_8]^{3+}$ and $[PdAu_8(PPh_3)_8]^{2+}$ (entry 1, Table 1) into a montmorillonite support to improve the stability during the catalytic usage.[54] The catalytic activity of the intercalated $[PdAu_8(PPh_3)_8]^{2+}$ was much higher than that of $[Au_9(PPh_3)_8]^{3+}$ for CO_2 hydrogenation. More interestingly, the reaction selectivity depended sharply on the central atom: $[Au_9(PPh_3)_8]^{3+}$ and $[PdAu_8(PPh_3)_8]^{2+}$ yielded methane and ethane as the major products, respectively. STEM analysis showed that the average diameter of the NCs on the spent catalyst increased to 2.2 nm from ~1 nm for the fresh catalyst.

3.4 Coupling reactions

Recently, Mandal *et al.* synthesized a novel Cu-doped Au NC $CuAu_{11}(PPh_3)_7Cl_2$ (entry 2, Table 1).[63] The Cu dopant was fully exposed and thus was expected to work as a reaction site for the catalysis. $CuAu_{11}(PPh_3)_7Cl_2$ exhibited high activity in the coupling reactions between 1-iodo-4-methylbenzene and various substituted phenylacetylenes (eqn (6)), while the undoped $Au_{11}(PPh_3)_7Cl_3$ was catalytically inert to these coupling reactions. In addition, $CuAu_{11}(PPh_3)_7Cl_2$ showed a high selectivity toward the Glaser coupling products, in sharp contrast to the Sonogashira coupling product by using $Au_{25}(PET)_{18}$. DFT calculations verified that the unsaturated Cu acted as a reaction site like a single-atom catalyst and kinetically favored Glaser coupling over Sonogashira coupling.

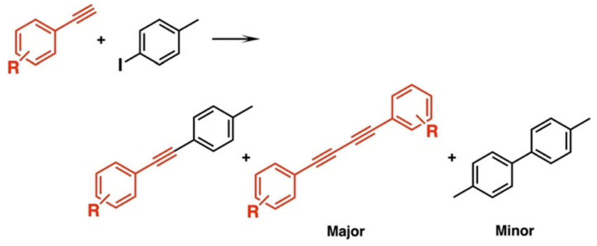

(6)

4 Electrocatalysis

4.1 Hydrogen evolution reaction (HER)

The single-atom doping effects on the catalysis of ligated Au/Ag NCs were investigated in the HER. Table 4 compares the catalytic performance under the specified experimental conditions in terms of onset potential (η) and current density.

Lee *et al.* reported that $PtAu_{24}(SC6)_{18}/C$ (entry 5, Table 1) showed a much higher reaction rate and turnover frequency (TOF) for the HER in a tetrahydrofuran (THF) solution of trifluoroacetic acid (TFA) than conventional molecular catalysts, and was even more reactive than the benchmark Pt/C (entry 1, Table 4) by depositing on the carbon support.[42] They further revealed that $PtAu_{24}(SC6)_{18}/C$ was superior to $PdAu_{24}(SC6)_{18}/C$ (entries 4 and 5, Table 1) as a catalyst for the HER (entry 2, Table 4).[47] The onset potentials of $PtAu_{24}(SC6)_{18}/C$ and $PdAu_{24}(SC6)_{18}/C$ were comparable (−0.07 V) (Fig. 3b) and similar to the first reduction potentials, indicating that the reduction potentials of the NCs have a significant impact on the emergence of the activity (Fig. 3a). Contrary to the expectations from this result, the TOF by $PtAu_{24}(SC6)_{18}/C$ was much higher than that by $PdAu_{24}(SC6)_{18}/C$ at any potential (Fig. 3b). The superior activity of $PtAu_{24}(SC6)_{18}/C$ over $PdAu_{24}(SC6)_{18}/C$ was explained by the hydrogen adsorption Gibbs free energy (ΔG_H) (Fig. 3c): ΔG_H was estimated to be 0.43, 0.36, and 0.31 eV for $Au_{25}(SC6)_{18}$, $PdAu_{24}(SC6)_{18}$, and $PtAu_{24}(SC6)_{18}$, respectively. The DFT-optimized structures for $PtAu_{24}(SC1)_{18}$ and $PdAu_{24}(SC1)_{18}$ suggested that hydrogen could be incorporated into the M@Au_{12} core (M = Pt, Pd), forming a H–M bond (Fig. 3d).

The HER in acidic media is known to start with hydrogen adsorption to the active site (*) (Volmer step, eqn (7a)).[105]

$$H^+ + e^- + * \rightarrow H* \tag{7a}$$

This step is followed by the production of H_2 *via* a heterolytic pathway between the adsorbed H (H*) and H^+ (Heyrovsky step,

Table 4 Summary of the electrolyte, onset potential, and current density in the HER for single-atom-doped Au/Ag nanoclusters

Entry	Catalyst	η (mV)	Current density (mA cm^{-2} mg^{-1})	Electrolyte	Ref.
1[a,b]	$PtAu_{24}(SC6)_{18}$/C/GDL	70	750 (−0.4 V *vs.* RHE)	1.0 M Britton–Robinson buffer solution (pH 3)	42
2[a,c]	$Au_{25}(SC6)_{18}$/C/GCE	200	239 (−0.6 V *vs.* RHE)	1.0 M Britton–Robinson buffer solution and 2.0 M KCl (pH 3)	47
	$PdAu_{24}(SC6)_{18}$/C/GCE	70	501 (−0.6 V *vs.* RHE)		
	$PtAu_{24}(SC6)_{18}$/C/GCE	70	870 (−0.6 V *vs.* RHE)		
3[d,e]	$Au_{25}(PET)_{18}$/C	562[g]	27.3 (−0.5 V *vs.* RHE)	0.5 M H_2SO_4	57
	$PtAu_{24}(PET)_{18}$/C	442[g]	N.A.		
	$Au_{25}(C{\equiv}CAr^F)_{18}$/C	490[g]	85.8 (−0.5 V *vs.* RHE)		
	$PtAu_{24}(C{\equiv}CAr^F)_{18}$/C	434[g]	N.A.		
4[c,f]	$Ag_{25}(SPhMe_2)_{18}$/C/GCE	250	2345 (−0.6 V *vs.* RHE)	1.0 M KOH	58
	$NiAg_{24}(SPhMe_2)_{18}$/C/GCE	50	4173 (−0.6 V *vs.* RHE)		

[a] SC6: hexanethiolate. [b] GDL: gas diffusion layer. [c] GCE: glassy carbon electrode. [d] PET: 2-phenylethanethiolate. [e] $HC{\equiv}CAr^F$: 3,5-bis(trifluoromethyl)ethynylbenzene. [f] $SPhMe_2$: 2,4-dimethylbenzenethiolate. [g] Overpotential at 10 mA cm^{-2} (η_{10})

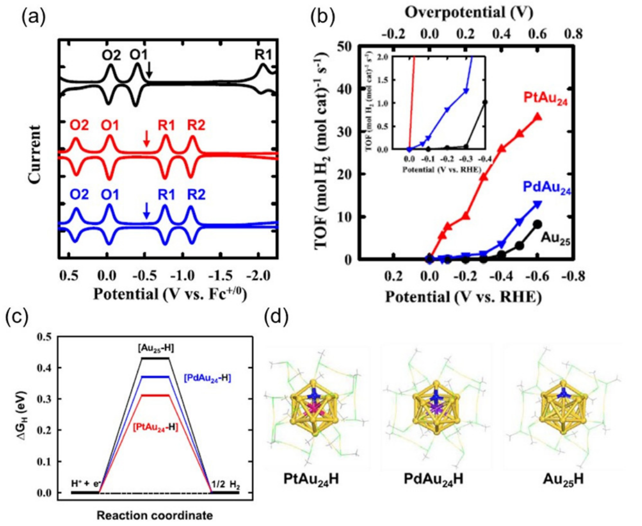

Fig. 3 (a) Square-wave voltammetry (SWV) of $MAu_{24}(SC6)_{18}$ with M = Au (black), Pt (red), and Pd (blue) in dichloromethane (1.0 mM). The arrows denote the open circuit potential of the NCs. (b) Turnover frequency (TOF) against the potential obtained from the constant potential electrolysis of the $MAu_{24}(SC6)_{18}$/C/gas diffusion layer electrode in 1.0 M Britton–Robinson buffer solution containing KCl (2.0 M). Inset: enlarged view of the low-overpotential region. (c) Hydrogen adsorption Gibbs free energy (ΔG_H) diagrams for $MAu_{24}(SCH_3)_{18}$ obtained by theoretical calculations and (d) DFT-optimised structures of H-$MAu_{24}(SCH_3)_{18}$. Color code; pink, Pt; purple, Pd; yellow, Au; blue, adsorbed H. Protection motifs are in the line view; green, S; gray, C; white, H. Reproduced from ref. 47 with permission from the American Chemical Society, Copyright 2018.

eqn (7b)) or a homolytic reaction between the two H* atoms (Tafel step, eqn (7c)):

$$H* + H^+ + e^- \rightarrow H_2 + * \quad (7b)$$

$$H* + H* \rightarrow H_2 + 2* \quad (7c)$$

Lee *et al.* proposed that the HER pathway was changed by single-atom doping: the HER by $Au_{25}(SC6)_{18}$/C proceeds *via* a homoleptic pathway (Scheme 5a), while that by $PtAu_{24}(SC6)_{18}$/C proceeds *via* a heterolytic pathway (Scheme 5b).

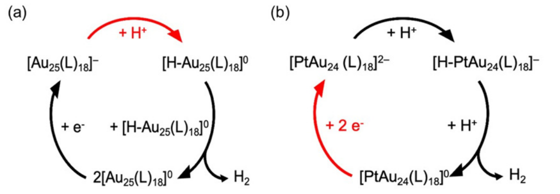

Scheme 5 HER cycle catalyzed by (a) $Au_{25}(SC6)_{18}$ and (b) $PtAu_{24}(SC6)_{18}$. The RDS is indicated by the red arrow. Reproduced from ref. 56 with permission from the American Chemical Society, Copyright 2021.

Tsukuda *et al.* revealed that the overpotential at 10 mA cm^{-2} (η_{10}) of $PtAu_{24}(PET)_{18}$/C (entry 5, Table 1) was lower compared to $Au_{25}(PET)_{18}$/C (entry 3, Table 4),[56] as observed in the case of $PtAu_{24}(SC6)_{18}$/C and $Au_{25}(SC6)_{18}$/C (entry 2, Table 4). The TOF value was more enhanced for $Au_{25}(C{\equiv}CAr^F)_{18}$/C ($Ar^F$: 3,5-bis(trifluoromethyl)-phenyl) than $Au_{25}(PET)_{18}$/C (entry 8, Table 1; entry 3, Table 4).[56] This remarkable ligand effect is explained in such a manner that the RDS (protonation of $[Au_{25}(PET)_{18}]^-$, Scheme 5a) is promoted by the alkynyl ligand layer having a more electron-rich nature than the thiolate ligand layer. However, the η_{10} value of $PtAu_{24}(C{\equiv}CAr^F)_{18}$/C was not significantly lowered compared to $Au_{25}(C{\equiv}CAr^F)_{18}$/C (entry 3, Table 4).[56] These results showed that the single-atom doping effects on HER activity depended on the nature of the ligand layer.

Lee *et al.* reported that $NiAg_{24}(SPhMe_2)_{18}$/C (entry 12, Table 1) in alkaline media showed higher HER activity than $Ag_{25}(SPhMe_2)_{18}$/C (entry 4, Table 4).[57] The HER in alkaline media begins with the dissociation of H_2O into adsorbed H (H*) and OH^- (Volmer step, eqn (8a)).[105]

$$H_2O + e^- + * \rightarrow H* + OH^- \quad (8a)$$

The adsorbed H* reacts with H_2O (Heyrovsky step, eqn (8b)) or recombines with the neighboring H* (Tafel step, eqn (8c)) to produce H_2.

$$H* + H_2O + e^- \rightarrow H_2 + OH^- + * \quad (8b)$$

$$H * + H* \rightarrow H_2 + 2* \tag{8c}$$

The onset potential for $NiAg_{24}(SPhMe_2)_{18}/C$ (−0.05 V) shifted to positive with respect to that for $Ag_{25}(SPhMe_2)_{18}/C$ (−0.25 V), signifying that the reduction potential is shifted positively upon Ni doping. The Tafel analysis indicated that Ni doping dramatically improved the Volmer step (eqn (8a)). DFT calculations of the dethiolated models $NiAg_{24}(SC1)_{17}$ and $Ag_{25}(SC1)_{17}$ further revealed that the hydrogen adsorption energy was substantially reduced upon Ni doping.

4.2 CO_2 electroreduction reaction (CO_2RR)

Since Au-based catalysts are known to show excellent selectivity in the CO_2 electroreduction reaction (CO_2RR, eqn (9a)–(9c)) to CO,[106,107] Au-based NCs are potential candidates for superior catalysts.

$$CO_2 + H^+ + e^- + * \rightarrow COOH* \tag{9a}$$

$$COOH * + H^+ + e^- + * \rightarrow CO * + H_2O \tag{9b}$$

$$CO* \rightarrow CO + * \tag{9c}$$

Table 5 compares the catalytic performance under the specified experimental conditions in terms of faradaic efficiency for CO (FE_{CO}) and CO partial current density (j_{CO}).

Jin *et al.* compared the catalytic activity of $PdAu_{24}(PET)_{18}/C$ and $Au_{25}(PET)_{18}/C$ for the CO_2RR. The CO partial mass activity of $PdAu_{24}(PET)_{18}/C$ was ∼2 times larger than that of $Au_{25}(PET)_{18}/C$ at −1.2 V (entry 1, Table 5 and Fig. 4a).[51] In addition, $PdAu_{24}(PET)_{18}/C$ maintained ∼100% FE_{CO} over a wide range of potential up to −1.2 V by suppressing unfavorable H_2 formation *via* the HER (Fig. 4b), while FE_{CO} of $Au_{25}(PET)_{18}/C$ started to decrease at −0.9 V. To identify the active site on $PdAu_{24}(PET)_{18}/C$, DFT calculations were conducted on two model systems, $MAu_{24}(SC1)_{17}$ and $MAu_{24}S(SC1)_{17}$, constructed by removing a CH_3S or CH_3 from $MAu_{24}(SC1)_{18}$ (M = Pd, Au; SC1 = SCH_3), respectively (Fig. 4c). The formation of a COOH* adsorbate from CO_2 was energetically unfavorable on the exposed Au site of $MAu_{24}(SC1)_{17}$ (blue and green in Fig. 4d), whereas the HER was favorable on such sites in $MAu_{24}(PET)_{17}$ (blue and green in Fig. 4e). On the other hand, the S site on $PdAu_{24}S(SC1)_{17}$ stabilized the COOH* intermediate (black in Fig. 4d) and had a large thermodynamic barrier for the HER (black in Fig. 4e), suggesting that the S site on $PdAu_{24}S(PET)_{17}$ was the reaction site for the selective CO_2RR.

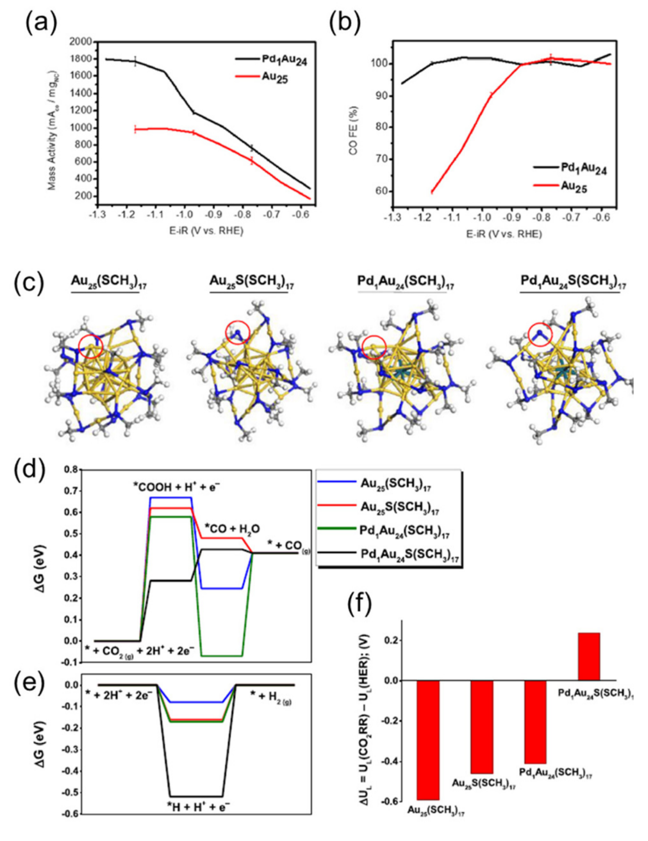

Fig. 4 (a) CO mass activity and (b) faradaic efficiency for CO in the CO_2RR over $Au_{25}(PET)_{18}/C$ and $PdAu_{24}(PET)_{18}/C$. (c) DFT-optimized structures of $MAu_{24}(SCH_3)_{18}$ and $MAu_{24}S(SCH_3)_{17}$ (M = Pd, Au). Proposed active sites are circled in red. Colour code: Au, yellow; Pd, turquoise; S, blue; C, gray; H, white. Gibbs free energy diagrams for the (d) CO_2RR and (e) HER at U = 0 V *vs.* RHE. (f) Difference in the predicted limiting potentials for the CO_2RR and HER. Reproduced from ref. 51 with permission from the American Chemical Society, Copyright 2020.

Lee *et al.* studied the CO_2RR by using $PtAu_{24}(PET)_{18}/C$ (entry 5, Table 1), which acted as the prominent catalyst for

Table 5 Summary of the electrolyte, faradaic efficiency of CO (FE_{CO}), and CO partial current density (j_{CO}) in the CO_2RR for single-atom-doped Au nanoclusters

Entry	Catalyst	FE_{CO}	j_{CO} (mA_{CO} cm^{-2})	Electrolyte	Ref.
1[a]	$Au_{25}(PET)_{18}/C$	∼100% (−0.9 V *vs.* RHE)	∼20 (−1.2 V *vs.* RHE)	0.1 M aqueous $KHCO_3$	52
	$PdAu_{24}(PET)_{18}/C$	∼100% (−1.2 V *vs.* RHE)	∼35.5 (−1.2 V *vs.* RHE)		
2[b,c]	$Au_{25}(SC6)_{18}/C/GCE$	∼95% (−0.3–−0.6 V *vs.* RHE)	12 (−1.0 V *vs.* RHE)	0.1 M aqueous $KHCO_3$ and 0.4 M KCl	56
	$PtAu_{24}(SC6)_{18}/C/GCE$	∼50% (−0.6–−0.8 V *vs.* RHE)	5 (−1.0 V *vs.* RHE)		
3[d]	$Au_{38}(SCH_2Ph^tBu)_{24}/C$	67% (−0.6 V *vs.* RHE)	2.5 (−0.6 V *vs.* RHE)	0.5 M aqueous $KHCO_3$	61
	$PtAu_{37}(SCH_2Ph^tBu)_{24}/C$	77% (−0.6 V *vs.* RHE)	7.0 (−0.6 V *vs.* RHE)		
	$Pt_2Au_{36}(SCH_2Ph^tBu)_{24}/C$	60% (−0.6 V *vs.* RHE)	1.4 (−0.6 V *vs.* RHE)		
4[a]	$Au_{25}(PET)_{18}/C$	40–70% (−0.3–−0.8 V *vs.* RHE)	7.0 (−0.6 V *vs.* RHE)	1 M aqueous $KHCO_3$	54
	$CdAu_{24}(PET)_{18}/C$	83–90% (−0.3–−0.8 V *vs.* RHE)	18.1 (−0.6 V *vs.* RHE)		

[a] PET: 2-phenylethanethiolate. [b] SC6: hexanethiolate. [c] GCE: glassy carbon electrode. [d] $HSCH_2Ph^tBu$: 4-*tert*-butylbenzyl mercaptan.

the HER.[55] $PtAu_{24}(PET)_{18}/C$ showed a moderate faradaic efficiency for H_2 (FE_{H_2}) even in the presence of CO_2, while $Au_{25}(PET)_{18}/C$ exhibited a high FE_{CO} at a lower potential (entry 2, Table 5). Theoretical calculations also supported the experimental trend in terms of thermodynamic stability. In addition, the limiting potential of $PtAu_{24}(PET)_{18}/C$ for the HER (0.09 eV) was much smaller than that for the CO_2RR (0.74 eV), whereas the limiting potential of $Au_{25}(PET)_{18}/C$ for the HER (0.32 eV) was higher than that for the CO_2RR (0.09 eV). Based on these findings, they demonstrated the production of syngas with controlled ratios of H_2/CO using a mixture of $Au_{25}(PET)_{18}/C$ and $PtAu_{24}(PET)_{18}/C$.

The single-atom or diatomic Pt doping effect on the CO_2RR for $Au_{38}(PET)_{24}$ having a biicosahedral Au_{23} core (entry 13, Table 1) was reported by Zhu *et al.* (entry 3, Table 5).[60] DFT calculations on model systems revealed that all the orbitals of $Pt_2Au_{36}(SH)_{24}$ and $Pt_1Au_{37}(SH)_{24}$ were stabilized and destabilized, respectively, with respect to those of $Au_{38}(SH)_{24}$. These results suggested that $Pt_1Au_{37}(SH)_{24}$ with the largest oxidation potential showed the highest activity in the CO_2RR. In fact, $Pt_1Au_{37}(PET)_{24}/C$ exhibited the best j_{CO} and FE_{CO} compared to the others. Gibbs free energy for adsorption of the COOH* intermediate supports the experimental trend: the free energy was estimated by DFT calculations to be 2.37, 2.22, and 2.40 eV for $Au_{38}(SH)_{24}$, $Pt_1Au_{37}(SH)_{24}$, and $Pt_2Au_{36}(SH)_{24}$, respectively. This study suggested that energy-level tuning had a large impact on the CO_2RR activity even if Pt, suitable for the HER, was used as a dopant.

The doping effect of Cd on the CO_2RR was investigated by Chen *et al.* (entry 4, Table 5) using $Au_{25}(PET)_{18}/C$, $CdAu_{24}(PET)_{18}/C$, $Au_{19}Cd_3(S\text{-tol})_{18}/C$ (S-tol: *p*-toluenethiolate), and $Au_{38}Cd_4(d\text{-MBT})_{30}/C$ (d-MBT: 3,5-dimethylthiophenolate) for comparison (entry 7, Table 1).[53] Among these catalysts, $CdAu_{24}(PET)_{18}/C$ exhibited the highest j_{CO} and FE_{CO} in all the potential ranges studied. They hypothesized that the difference in the catalysis rose from that of active sites formed by S–C or M–S bond (M: metal) cleavage in the ligand layer. DFT calculations showed that the S–C bond cleavage of $CdAu_{24}(SR)_{18}$ leads to an open S site, which can efficiently bind CO_2 for the CO_2RR. They also investigated the effect of the R group on the catalysis of $CdAu_{24}(SR)_{18}/C$. $CdAu_{24}(S\text{-}n\text{Bu})_{18}/C$ (S-*n*Bu: 1-butanethiolate) showed a better j_{CO} and FE_{CO} than $CdAu_{24}(PET)_{18}/C$: the DFT calculations predicted that the S–C bond of S-*n*Bu was more easily dissociated than that of PET. Cd doping into $Au_{25}(PET)_{18}$ promoted the formation of active S sites at lower potentials due to the lower dissociation energy of the S–C bonds close to the Cd atom, thus enhancing the activity and selectivity for the CO_2RR.

4.3 Other reactions

The single-atom doping effects were studied for the oxygen evolution reactions (OER, eqn (10)) and oxygen reduction reactions (ORRs, eqn (11a) and (11b)) in an acidic electrolyte.

$$2H_2O \rightarrow O_2 + 4H^+ + 4e^- \tag{10}$$

$$O_2 + 4H^+ + 4e^- \rightarrow 2H_2O \tag{11a}$$

$$O_2 + 2H^+ + 2e^- \rightarrow H_2O_2 \tag{11b}$$

Negishi *et al.* found that $PdAu_{24}(PET)_{18}/C$ showed higher activity than $Au_{25}(PET)_{18}/C$ for the OER and ORR.[52]

Chen *et al.* examined the single-atom doping effect for formic acid electrooxidation (FAO, eqn (12)).[48]

$$HCOOH + * \rightarrow CO_2 + * + 2H^+ + 2e^- \tag{12}$$

Although $Au_{25}(SC12)_{18}/MCNT$ (MCNT = multi-wall carbon nanotube) did not catalyze FAO, $PtAu_{24}(SC12)_{18}/MCNT$ catalyzed FAO without the formation of the unfavorable side product CO, and exhibited a current density about 12 and 34 times higher than that of C12S-protected Pt NC/MCNT and commercial Pt/C, respectively. The enhanced activity by Pt doping was ascribed to the modulation of the electronic structure, and the complete suppression of the formation of the poisoning CO intermediate was due to the protection of the Pt dopant at the center of the $PtAu_{12}$ core. Based on the DFT-calculated potential-dependent free energies and kinetics, they proposed that the FAO on $PtAu_{24}(SC12)_{18}/MCNTs$ proceeds exclusively *via* the direct pathway with COOH as the preferred reactive intermediate:

$$HCOOH + * \rightarrow COOH* + H^+ + e^- \tag{12a}$$

$$COOH* \rightarrow CO_2* + H^+ + e^- \tag{12b}$$

$$CO_2* \rightarrow CO_2 + * \tag{12c}$$

5 Photocatalysis

5.1 Photocatalytic HER and OER for water splitting

In contrast to mature research on photocatalytic water splitting,[108] there have been few applications of Au/Ag NCs in photocatalysis. We herein highlight some examples showing the potential of the Au/Ag NCs as cocatalysts of photocatalytic materials and the improvement of their performance by single-atom doping with other metals.

Yang *et al.* used $MAg_{24}(SPhMe_2)_{18}$ (M = Ag, Pt) (entry 11, Table 1) as a cocatalyst of the visible-light-driven photocatalytic HER by using a graphitic carbon nitride ($g\text{-}C_3N_4$) with a narrow band gap (2.7–2.9 eV).[43] $PtAg_{24}(SPhMe_2)_{18}/g\text{-}C_3N_4$ was 5.2 times superior to $Ag_{25}(SPhMe_2)_{18}/g\text{-}C_3N_4$, while the calcined $PtAg_{24}/g\text{-}C_3N_4$ (entry 2, Table 3) showed 4.4 times higher activity than $Ag_{25}/g\text{-}C_3N_4$. These results indicated that single-Pt atom doping was advantageous regardless of annealing. Photoelectrochemical characterization studies revealed that doping with a Pt atom improved the electron transfer efficiency and thus led to high activity.

Negishi *et al.* investigated water-splitting catalysis by using a Au_{25} NC supported on a semiconductor $BaLa_4Ti_4O_{15}$ under UV light.[49] $Au_{24}M(PET)_{18-x}(p\text{MBA})_x$ (M = Pd, Pt, Au) (entries 4 and 5, Table 1) supported on $BaLa_4Ti_4O_{15}$ was calcined *in vacuo* at 300 °C for 80 min (Fig. 5a, entries 3 and 4, Table 3) to

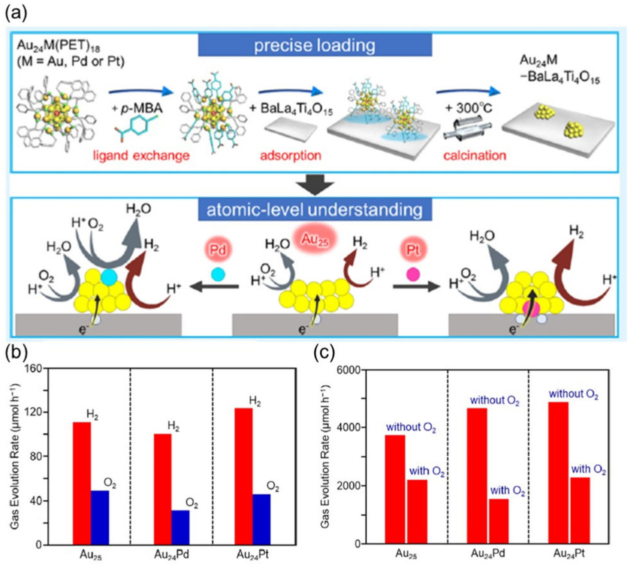

Fig. 5 (a) Schematic illustration of the synthesis procedure for the $Au_{24}M/BaLa_4Ti_4O_{15}$ photocatalyst (M = Au, Pd, or Pt) and the role of the dopant in the HER. (b) Hydrogen and oxygen evolution rates for Au_{25}, $Au_{24}Pd$ and $Au_{24}Pt$ in photocatalytic water splitting under UV light. (c) Difference in the hydrogen evolution rate in the presence of methanol as a sacrificial reagent under a flow of Ar gas (without O_2) and a 7 : 3 mixture ratio of Ar to air (with O_2). Reproduced from ref. 49 with permission from the American Chemical Society, Copyright 2019.

remove PET and *p*MBA. Pd–K or Pt–L_3 edge XAFS of the calcined catalysts suggested that Pd was located on the surface of the Au_{24} NC, while Pt was located at the interface between the NC and $BaLa_4Ti_4O_{15}$ (Fig. 5a). $Au_{24}M/BaLa_4Ti_4O_{15}$ (M = Pt, Pd) showed higher and lower activity than the undoped $Au_{25}/BaLa_4Ti_4O_{15}$, respectively, in the water-splitting reaction (Fig. 5b). In contrast, $Au_{24}M/BaLa_4Ti_4O_{15}$ (M = Pt, Pd) improved the reaction rates for the photocatalytic HER using methanol as a sacrificial reagent (Fig. 5c). The reaction was slowed to some extent for all the catalysts in the presence of O_2 (Fig. 5c). These results suggested that Pd and Pt dopants played different roles in the water-splitting activity: $Au_{24}Pd/BaLa_4Ti_4O_{15}$ catalyzed the photocatalytic ORR more than the photocatalytic HER, while the $PtAu_{24}$ catalyst facilitated the photocatalytic HER more than the photocatalytic ORR.

Wang *et al.* compared the photocatalytic HER activity of $MAg_{24}(SPhMe_2)_{18}/TiO_2$ (M = Au, Pd, Pt) (entries 9–11, Table 1).[62] The undoped $Ag_{25}(SPhMe_2)_{18}/TiO_2$ showed the highest activity, which was explained in terms of the M-dependent energy levels of the orbitals. The LUMO levels for M = Au and Pd were located above the conduction band minimum (CBM) of TiO_2. Therefore, the photoexcited electron was not transferred from TiO_2 to the NCs, leading to the suppression of activity. In contrast, the electron transfer from $MAg_{24}(SPhMe_2)_{18}$ with M = Ag and Pt to TiO_2 was suppressed because their LUMO levels were located below the CBM of TiO_2. This explains the trend in the photocatalytic HER activity.

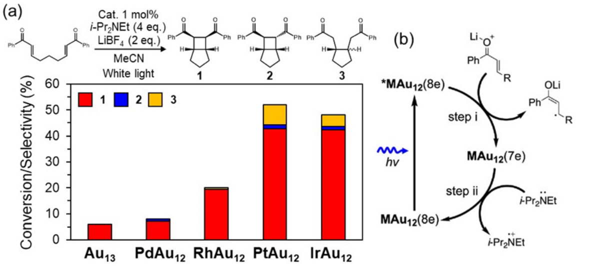

Fig. 6 (a) Comparison of the photoredox catalytic properties of $MAu_{12}(dppe)_5Cl_2$ (**MAu_{12}**; M = Au, Pd, Pt, Rh, or Ir). (b) Proposed reaction mechanism for **MAu_{12}**, a so-called oxidative quenching cycle. Reproduced from ref. 58 with permission from Wiley-VCH, Copyright 2023.

5.2 Photoredox catalysts

Successful application of the ligated metal NCs as a photosensitizer[109,110] suggests that they can catalyze the photocatalytic reactions. $MAu_{12}(dppe)_5Cl_2$ (M = Pt, Ir) in the electronically excited state had a lifetime of the μs timescale, leading to a remarkable photoluminescence quantum yield (PLQY) of >60% under deaerated conditions.[95] Recently, Tsukuda *et al.* applied a series of $MAu_{12}(dppe)_5Cl_2$ (M = Au, Pd, Pt, Rh, Ir) (entry 3, Table 1) for photoinduced intermolecular [2 + 2] cycloaddition of bisenone in the presence of $LiBF_4$ (Lewis acid) and i-Pr_2NEt (sacrificial reagent) as a model reaction.[58] They found that $MAu_{12}(dppe)_5Cl_2$ (M = Pt, Ir) with a high PLQY showed higher catalytic activity than $MAu_{12}(dppe)_5Cl_2$ (M = Au, Pd, Rh) (Fig. 6a), indicating that the electronically excited state was involved in the catalysis. It was proposed that the reaction proceeded in an oxidative quenching cycle (Fig. 6b): the electronically excited $^*MAu_{12}(8e)$ reduced bisenone to form $MAu_{12}(7e)$, which then oxidized *i*-Pr_2NEt to recover the initial $MAu_{12}(8e)$. This mechanism contrasts with the reductive quenching cycle found in the conventional $[Ru(bpy)_3]^{2+}$ (bpy: 2,2′-bipyridine) system.

6 Conclusion and outlook

This minireview summarized the synthesis, structural characterization, and catalytic application of SAD Au/Ag NCs. The SAD Au/Ag NCs introduced here have undoped counterparts composed of the same number of atoms. Furthermore, identical geometric structures of these pairs were demonstrated by SCXRD and predicted by DFT calculations. These situations provide novel opportunities to study how the catalysis is affected by replacing a single Au/Ag atom of the NCs with a dopant atom M. All SAD Au/Ag NCs showed significant single-atom doping effects on the catalytic properties of Au/Ag NCs. The role of a particular dopant M in catalysis depends largely on its location, which is governed by its interaction with the surrounding environment of the SAD Au/Ag NC. In many cases, dopants on the NC surface facilitate catalytic reactions by taking advantage of their inherently greater chemical reactivity toward small reacting molecules than that on the Au/Ag surface. In contrast, dopants located inside the NC promote catalytic reactions by modulating the electronic structure (*e.g.*, HOMO–LUMO gap, redox potential, excited state lifetime, *etc.*). These simple explanations provide practical hints for designing and creating active and selective NC catalysts through doping.

Nevertheless, several questions remain to be answered to better understand the doping effects in catalysis. (1) The most important and straightforward question is: Is there any synergistic effect between dopant M and the matrix NCs? In other words, do the chemical properties of the dopant M site and underlying NC surface change through electronic interactions? One way to address such synergistic effects is to compare the catalytic properties of M-doped NCs with those of pure M NCs. We recently reported that the Pd dopant in $Au_{23}Pd_1$ exhibited significantly higher catalytic activity than Pd NPs (1.6 nm) and Pd NPs (2.5 nm), which we attribute to the higher electronegativity of Pd in Pd_1Au_{23} than in Pd NPs. (2) The second question is: How does the structural fluxionality of SAD metal NCs affect their catalytic properties? For example, the structural strain induced by dopants with different atomic radii will affect the electronic structure of the matrix NC. Dynamic structural changes, including M diffusion, induced by the chemisorption of the reactants or thermal excitation, result in the fluctuation of the electronic structure of the mother NC. To answer these challenging questions, *in situ* structural characterization is necessary.

In addition, the following synthetic challenges for each type of SAD metal NC should be tackled. (1) An inherent problem in applying the ligand-protected SAD metal NCs for thermal reactions is the poor reactivity due to surface poisoning by the ligands. Thus, a challenge to overcome this problem is to design and create open sites. One approach is to reduce the surface coverage *via* steric hindrance between the adjacent ligands. Successful examples can be found in $[Au_{23}(Ph_3P)_{10}(dpa)_2Cl]^{2+}$ (dpa = dipyridylamide)[111] and $Au_{44}(NHC^{iPr})_9(C{\equiv}CPh)_6Br_8$ (NHC^{iPr} = 1,3-diisopropylbenzimidazolin-2-ylidene),[112] which have uncoordinated Au atoms on the surface and show excellent catalytic activity in the alcohol oxidation reaction and hydration of alkynes, respectively. By applying this approach to SAD metal NCs, it would be possible to construct NC catalysts with atomically designed reaction sites for active and selective catalysis. (2) A problem in the linear-polymer-stabilized SAD metal NCs is the uncontrollability of their size and insufficient stability under catalytic conditions. One approach for overcoming these problems is to use dendrimers as a container. The NC size can be controlled by the number of metal ions initially coordinated within the dendrimer. The stability of the resulting NCs in the dendrimer would be higher than that of the NCs stabilized by linear polymers, because the former is sterically encapsulated within the cavity of the dendrimers. Yamamoto *et al.* successfully synthesized and characterized alloy NCs using their original dendrimers.[113] (3) An inherent issue of the solid-supported SAD metal NCs is the uncontrollability of the geometric structures. This problem can be solved by using molecular metal oxides such as polyoxometalates as a support. Suzuki and Yamaguchi successfully obtained atomically precise Ag NCs with well-defined structures and exposed surfaces, such as $[Ag_7(Si_3W_{27}O_{96})]$,[114] $[Ag_{27}(Si_6W_{54}O_{198})]$,[115] and $[Ag_{30}(P_8W_{48}O_{184})]$.[116] There is also room for improving robustness under harsh reaction conditions. Masuda and Tsukuda improved the robustness of Au_{25} catalysts by intentionally and selectively leaving the thiolates located at the interface with the carbon support.[117] Multiple van der Waals interactions between the ligands and the carbon support immobilized the Au_{25} NCs. Application of these approaches may realize supported SAD metal NCs with atomically defined structures.

By solving the challenges listed above, we can expand the scope and deepen our understanding of the doping effects on catalysis. The basic knowledge with the help of an AI-based machine learning approach will accelerate the development of on-demand alloy catalysts in the future.

Author contributions

S. M. and T. T. prepared the draft of the manuscript. S. M. and K. S. summarized the related papers and wrote the manuscript. T. T. revised the manuscript prior to submission.

Note added in proof

An expression of concern for the chemical composition in Ref. 63 has been issued (S. E. Skrabalak, *Chem. Mater.*, 2023, **35**, 9817).

Conflicts of interest

There are no conflicts to declare.

Acknowledgements

This research was financially supported by JST, CREST (grant no. JPMJCR20B2) and a grant-in-aid for Scientific Research (A) (grant no. JP23H00284) and for Early-Career Scientists (grant no. JP23K13617) from the Japan Society for the Promotion of Science (JSPS).

References

1 N. T. S. Phan, M. Van Der Sluys and C. W. Jones, *Adv. Synth. Catal.*, 2006, **348**, 609–679.

2 T. Tsukuda, H. Tsunoyama and H. Sakurai, *Chem. – Asian J.*, 2011, **6**, 736–748.

3 L. Liu and A. Corma, *Chem. Rev.*, 2018, **118**, 4981–5079.

4 C. Mondelli, G. Gözaydın, N. Yan and J. Pérez-Ramírez, *Chem. Soc. Rev.*, 2020, **49**, 3764–3782.

5 M. R. Axet and K. Philippot, *Chem. Rev.*, 2020, **120**, 1085–1145.

6 V. Ponec, *Appl. Catal., A*, 2001, **222**, 31–45.

7 H. Miura and T. Shishido, *Chem. Lett.*, 2021, **50**, 346–352.

8 M. Zhou, C. Li and J. Fang, *Chem. Rev.*, 2021, **121**, 736–795.

9 J. W. M. Crawley, I. E. Gow, N. Lawes, I. Kowalec, L. Kabalan, C. R. A. Catlow, A. J. Logsdail, S. H. Taylor, N. F. Dummer and G. J. Hutchings, *Chem. Rev.*, 2022, **122**, 6795–6849.

10 L. Liu and A. Corma, *Chem. Rev.*, 2023, **123**, 4855–4933.

11 Y. Nakaya and S. Furukawa, *Chem. Rev.*, 2023, **123**, 5859–5947.

12 R. Jin, C. Zeng, M. Zhou and Y. Chen, *Chem. Rev.*, 2016, **116**, 10346–10413.

13 I. Chakraborty and T. Pradeep, *Chem. Rev.*, 2017, **117**, 8208–8271.

14 J. Yan, B. K. Teo and N. Zheng, *Acc. Chem. Res.*, 2018, **51**, 3084–3093.

15 Q. Yao, T. Chen, X. Yuan and J. Xie, *Acc. Chem. Res.*, 2018, **51**, 1338–1348.

16 Z. Lei, X.-K. Wan, S.-F. Yuan, Z.-J. Guan and Q.-M. Wang, *Acc. Chem. Res.*, 2018, **51**, 2465–2474.

17 A. Ghosh, O. F. Mohammed and O. M. Bakr, *Acc. Chem. Res.*, 2018, **51**, 3094–3103.

18 X. Kang, H. Chong and M. Zhu, *Nanoscale*, 2018, **10**, 10758–10834.

19 S. Wang, Q. Li, X. Kang and M. Zhu, *Acc. Chem. Res.*, 2018, **51**, 2784–2792.

20 W. W. Xu, X. C. Zeng and Y. Gao, *Acc. Chem. Res.*, 2018, **51**, 2739–2747.

21 K. Kwak and D. Lee, *Acc. Chem. Res.*, 2019, **52**, 12–22.

22 H. Hirai, S. Ito, S. Takano, K. Koyasu and T. Tsukuda, *Chem. Sci.*, 2020, **11**, 12233–12248.

23 X. Kang, Y. Li, M. Zhu and R. Jin, *Chem. Soc. Rev.*, 2020, **49**, 6443–6514.

24 T. Kawawaki, Y. Imai, D. Suzuki, S. Kato, I. Kobayashi, T. Suzuki, R. Kaneko, S. Hossain and Y. Negishi, *Chem. – Eur. J.*, 2020, **26**, 16150–16193.

25 S. Takano and T. Tsukuda, *J. Am. Chem. Soc.*, 2021, **143**, 1683–1698.

26 T. Omoda, S. Takano and T. Tsukuda, *Small*, 2021, **17**, 2001439.

27 T. Kawawaki, A. Ebina, Y. Hosokawa, S. Ozaki, D. Suzuki, S. Hossain and Y. Negishi, *Small*, 2021, **17**, 2005328.

28 Y. Liu, J. Yu, Y. Lun, Y. Wang, Y. Wang and S. Song, *Adv. Funct. Mater.*, 2023, **33**, 2304184.

29 A. V. Artem'ev and C. W. Liu, *Chem. Commun.*, 2023, **59**, 7182–7195.

30 H. Liang, Q. Chen, Q.-L. Mo, Y. Wu and F.-X. Xiao, *J. Mater. Chem. A*, 2023, **11**, 9401–9426.

31 M. F. Matus and H. Häkkinen, *Nat. Rev. Mater.*, 2023, **8**, 372–389.

32 S. Hossain, D. Hirayama, A. Ikeda, M. Ishimi, S. Funaki, A. Samanta, T. Kawawaki and Y. Negishi, *Aggregate*, 2023, **4**, e255.

33 Y. Li and R. Jin, *Nanoscale Horiz.*, 2023, **8**, 991–1013.

34 G. Giannakakis, M. Flytzani-Stephanopoulos and E. C. H. Sykes, *Acc. Chem. Res.*, 2019, **52**, 237–247.

35 R. T. Hannagan, G. Giannakakis, M. Flytzani-Stephanopoulos and E. C. H. Sykes, *Chem. Rev.*, 2020, **120**, 12044–12088.

36 T. Zhang, A. G. Walsh, J. Yu and P. Zhang, *Chem. Soc. Rev.*, 2021, **50**, 569–588.

37 T. Shen, S. Wang, T. Zhao, Y. Hu and D. Wang, *Adv. Energy Mater.*, 2022, **12**, 2201823.

38 J. D. Lee, J. B. Miller, A. V. Shneidman, L. Sun, J. F. Weaver, J. Aizenberg, J. Biener, J. A. Boscoboinik, A. C. Foucher, A. I. Frenkel, J. E. S. van der Hoeven, B. Kozinsky, N. Marcella, M. M. Montemore, H. T. Ngan, C. R. O'Connor, C. J. Owen, D. J. Stacchiola, E. A. Stach, R. J. Madix, P. Sautet and C. M. Friend, *Chem. Rev.*, 2022, **122**, 8758–8808.

39 S. Xie, H. Tsunoyama, W. Kurashige, Y. Negishi and T. Tsukuda, *ACS Catal.*, 2012, **2**, 1519–1523.

40 H. Qian, D.-E. Jiang, G. Li, C. Gayathri, A. Das, R. R. Gil and R. Jin, *J. Am. Chem. Soc.*, 2012, **134**, 16159–16162.

41 N. Yan, L. Liao, J. Yuan, Y.-J. Lin, L.-H. Weng, J. Yang and Z. Wu, *Chem. Mater.*, 2016, **28**, 8240–8247.

42 K. Kwak, W. Choi, Q. Tang, M. Kim, Y. Lee, D.-E. Jiang and D. Lee, *Nat. Commun.*, 2017, **8**, 14723.

43 X. L. Du, X. L. Wang, Y. H. Li, Y. L. Wang, J. J. Zhao, L. J. Fang, L. R. Zheng, H. Tong and H. G. Yang, *Chem. Commun.*, 2017, **53**, 9402–9405.

44 S. Hayashi, R. Ishida, S. Hasegawa, S. Yamazoe and T. Tsukuda, *Top. Catal.*, 2018, **61**, 136–141.

45 S. Hasegawa, S. Takano, S. Yamazoe and T. Tsukuda, *Chem. Commun.*, 2018, **54**, 5915–5918.

46 Y. Liu, X. Chai, X. Cai, M. Chen, R. Jin, W. Ding and Y. Zhu, *Angew. Chem., Int. Ed.*, 2018, **57**, 9775–9779.

47 W. Choi, G. Hu, K. Kwak, M. Kim, D.-E. Jiang, J.-P. Choi and D. Lee, *ACS Appl. Mater. Interfaces*, 2018, **10**, 44645–44653.

48 Y. Lu, C. Zhang, X. Li, A. R. Frojd, W. Xing, A. Z. Clayborne and W. Chen, *Nano Energy*, 2018, **50**, 316–322.

49 W. Kurashige, R. Hayashi, K. Wakamatsu, Y. Kataoka, S. Hossain, A. Iwase, A. Kudo, S. Yamazoe and Y. Negishi, *ACS Appl. Energy Mater.*, 2019, **2**, 4175–4187.

50 J. Xu, S. Xu, M. Chen and Y. Zhu, *Nanoscale*, 2020, **12**, 6020–6028.

51 S. Li, D. Alfonso, A. V. Nagarajan, S. D. House, J. C. Yang, D. R. Kauffman, G. Mpourmpakis and R. Jin, *ACS Catal.*, 2020, **10**, 12011–12016.

52 B. Kumar, T. Kawawaki, N. Shimizu, Y. Imai, D. Suzuki, S. Hossain, L. V. Nair and Y. Negishi, *Nanoscale*, 2020, **12**, 9969–9979.

53 Y. Sun, X. Liu, K. Xiao, Y. Zhu and M. Chen, *ACS Catal.*, 2021, **11**, 11551–11560.

54 X. Cai, X. Sui, J. Xu, A. Tang, X. Liu, M. Chen and Y. Zhu, *CCS Chem.*, 2021, **3**, 408–420.

55 W. Choi, H. Seong, V. Efremov, Y. Lee, S. Im, D.-H. Lim, J. S. Yoo and D. Lee, *J. Chem. Phys.*, 2021, **155**, 014305.

56 X. Li, S. Takano and T. Tsukuda, *J. Phys. Chem. C*, 2021, **125**, 23226–23230.

57 Y. Jo, M. Choi, M. Kim, J. S. Yoo, W. Choi and D. Lee, *Bull. Korean Chem. Soc.*, 2021, **42**, 1672–1677.

58 H. Hirai, S. Takano, T. Nakashima, T. Iwasa, T. Taketsugu and T. Tsukuda, *Angew. Chem., Int. Ed.*, 2022, **61**, e202207290.

59 S. Hasegawa, S. Masuda, S. Takano, K. Harano, J. Kikkawa and T. Tsukuda, *ACS Nano*, 2022, **16**, 16932–16940.

60 X. Liu, E. Wang, M. Zhou, Y. Wan, Y. Zhang, H. Liu, Y. Zhao, J. Li, Y. Gao and Y. Zhu, *Angew. Chem., Int. Ed.*, 2022, **61**, e202207685.

61 Y. Li, H. K. Kim, R. D. McGillicuddy, S.-L. Zheng, K. J. Anderton, G. J. Stec, J. Lee, D. Cui and J. A. Mason, *J. Am. Chem. Soc.*, 2023, **145**, 9304–9312.

62 Y. Liu, D. Long, A. Springer, R. Wang, N. Koch, M. Schwalbe, N. Pinna and Y. Wang, *Sol. RRL*, 2023, **7**, 2201057.

63 S. Mukherjee, A. Das, A. K. Das, A. Sheriff, K. Sunny, A. S. Nair, S. Bhandary, R. Bhowal, D. Chopra, B. Pathak, S. Yamazoe and S. Mandal, *Chem. Mater.*, 2023, **35**, 1659–1666.

64 P. D. Jadzinsky, G. Calero, C. J. Ackerson, D. A. Bushnell and R. D. Kornberg, *Science*, 2007, **318**, 430–433.

65 M. W. Heaven, A. Dass, P. S. White, K. M. Holt and R. W. Murray, *J. Am. Chem. Soc.*, 2008, **130**, 3754–3755.

66 M. Zhu, C. M. Aikens, F. J. Hollander, G. C. Schatz and R. Jin, *J. Am. Chem. Soc.*, 2008, **130**, 5883–5885.

67 J. Yan, H. Su, H. Yang, S. Malola, S. Lin, H. Häkkinen and N. Zheng, *J. Am. Chem. Soc.*, 2015, **137**, 11880–11883.

68 M. S. Bootharaju, C. P. Joshi, M. R. Parida, O. F. Mohammed and O. M. Bakr, *Angew. Chem., Int. Ed.*, 2016, **55**, 922–926.

69 S. Takano, S. Ito and T. Tsukuda, *J. Am. Chem. Soc.*, 2019, **141**, 15994–16002.

70 W. Fei, S. Antonello, T. Dainese, A. Dolmella, M. Lahtinen, K. Rissanen, A. Venzo and F. Maran, *J. Am. Chem. Soc.*, 2019, **141**, 16033–16045.

71 S. Yamazoe, T. Yoskamtorn, S. Takano, S. Yadnum, J. Limtrakul and T. Tsukuda, *Chem. Rec.*, 2016, **16**, 2338–2348.

72 S. Yamazoe and T. Tsukuda, *Bull. Chem. Soc. Jpn.*, 2018, **92**, 193–204.

73 S. Hasegawa, S. Takano, K. Harano and T. Tsukuda, *JACS Au*, 2021, **1**, 660–668.

74 S. Hasegawa, S. Masuda, S. Takano, K. Harano and T. Tsukuda, *ACS Catal.*, 2022, **12**, 6550–6558.

75 Y. Negishi, W. Kurashige, Y. Niihori, T. Iwasa and K. Nobusada, *Phys. Chem. Chem. Phys.*, 2010, **12**, 6219–6225.

76 A. Bruma, F. R. Negreiros, S. Xie, T. Tsukuda, R. L. Johnston, A. Fortunelli and Z. Y. Li, *Nanoscale*, 2013, **5**, 9620–9625.

77 S. Zhao, R. Jin and R. Jin, *ACS Energy Lett.*, 2018, **3**, 452–462.

78 J. Zhao and R. Jin, *Nano Today*, 2018, **18**, 86–102.

79 T. Higaki, Y. Li, S. Zhao, Q. Li, S. Li, X.-S. Du, S. Yang, J. Chai and R. Jin, *Angew. Chem., Int. Ed.*, 2019, **58**, 8291–8302.

80 Y. Du, H. Sheng, D. Astruc and M. Zhu, *Chem. Rev.*, 2020, **120**, 526–622.

81 R. Jin, G. Li, S. Sharma, Y. Li and X. Du, *Chem. Rev.*, 2021, **121**, 567–648.

82 T. Kawawaki, Y. Kataoka, M. Hirata, Y. Iwamatsu, S. Hossain and Y. Negishi, *Nanoscale Horiz.*, 2021, **6**, 409–448.

83 S. Li, W. Tian and Y. Liu, *Nanoscale*, 2021, **13**, 16847–16859.

84 A. G. Walsh and P. Zhang, *Adv. Mater. Interfaces*, 2021, **8**, 2001342.

85 X. Cai, Y. Sun, J. Xu and Y. Zhu, *Chem. – Eur. J.*, 2021, **27**, 11539–11547.

86 X. Cai, G. Li, W. Hu and Y. Zhu, *ACS Catal.*, 2022, **12**, 10638–10653.

87 D. Yang, J. Wang, Q. Wang, Z. Yuan, Y. Dai, C. Zhou, X. Wan, Q. Zhang and Y. Yang, *ACS Nano*, 2022, **16**, 15681–15704.

88 W. Jing, H. Shen, R. Qin, Q. Wu, K. Liu and N. Zheng, *Chem. Rev.*, 2023, **123**, 5948–6002.

89 X. Liu, X. Cai and Y. Zhu, *Acc. Chem. Res.*, 2023, **56**, 1528–1538.

90 S. N. Khanna and P. Jena, *Phys. Rev. Lett.*, 1992, **69**, 1664–1667.

91 S. N. Khanna and P. Jena, *Phys. Rev. B: Condens. Matter Mater. Phys.*, 1995, **51**, 13705–13716.

92 P. Jena and Q. Sun, *Chem. Rev.*, 2018, **118**, 5755–5870.

93 C. Garcia, V. Truttmann, I. Lopez, T. Haunold, C. Marini, C. Rameshan, E. Pittenauer, P. Kregsamer, K. Dobrezberger, M. Stöger-Pollach, N. Barrabés and G. Rupprechter, *J. Phys. Chem. C*, 2020, **124**, 23626–23636.

94 S. Takano, H. Hirai, S. Muramatsu and T. Tsukuda, *J. Am. Chem. Soc.*, 2018, **140**, 12314–12317.

95 H. Hirai, S. Takano, T. Nakamura and T. Tsukuda, *Inorg. Chem.*, 2020, **59**, 17889–17895.

96 D. R. Alfonso, D. Kauffman and C. Matranga, *J. Chem. Phys.*, 2016, **144**, 184705.

97 N. Austin, S. Zhao, J. R. McKone, R. Jin and G. Mpourmpakis, *Catal. Sci. Technol.*, 2018, **8**, 3795–3805.

98 S. Zhao, N. Austin, M. Li, Y. Song, S. D. House, S. Bernhard, J. C. Yang, G. Mpourmpakis and R. Jin, *ACS Catal.*, 2018, **8**, 4996–5001.

99 H. Seong, V. Efremov, G. Park, H. Kim, J. S. Yoo and D. Lee, *Angew. Chem., Int. Ed.*, 2021, **60**, 14563–14570.

100 F. Sun, L. Qin, Z. Tang, G. Deng, M. S. Bootharaju, Z. Wei, Q. Tang and T. Hyeon, *Chem. Sci.*, 2023, **14**, 10532–10546.

101 O. López-Estrada, N. Mammen, L. Laverdure, M. M. Melander, H. Häkkinen and K. Honkala, *ACS Catal.*, 2023, **13**, 8997–9006.

102 T. Imaoka, R. Tanaka, S. Arimoto, M. Sakai, M. Fujii and K. Yamamoto, *J. Am. Chem. Soc.*, 2005, **127**, 13896–13905.

103 K. Yamamoto and T. Imaoka, *Acc. Chem. Res.*, 2014, **47**, 1127–1136.

104 V. Sudheeshkumar, K. O. Sulaiman and R. W. J. Scott, *Nanoscale Adv.*, 2020, **2**, 55–69.

105 N. Mahmood, Y. Yao, J.-W. Zhang, L. Pan, X. Zhang and J.-J. Zou, *Adv. Sci.*, 2018, **5**, 1700464.

106 D. R. Kauffman, D. Alfonso, C. Matranga, H. Qian and R. Jin, *J. Am. Chem. Soc.*, 2012, **134**, 10237–10243.

107 W. Zhu, R. Michalsky, Ö. Metin, H. Lv, S. Guo, C. J. Wright, X. Sun, A. A. Peterson and S. Sun, *J. Am. Chem. Soc.*, 2013, **135**, 16833–16836.

108 Z. Wang, C. Li and K. Domen, *Chem. Soc. Rev.*, 2019, **48**, 2109–2125.

109 H. Kawasaki, S. Kumar, G. Li, C. Zeng, D. R. Kauffman, J. Yoshimoto, Y. Iwasaki and R. Jin, *Chem. Mater.*, 2014, **26**, 2777–2788.

110 K. Isozaki, R. Ueno, K. Ishibashi, G. Nakano, H. Yin, K. Iseri, M. Sakamoto, H. Takaya, T. Teranishi and M. Nakamura, *ACS Catal.*, 2021, **11**, 13180–13187.

111 S.-F. Yuan, Z. Lei, Z.-J. Guan and Q.-M. Wang, *Angew. Chem., Int. Ed.*, 2021, **60**, 5225–5229.

112 H. Shen, Z. Xu, M. S. A. Hazer, Q. Wu, J. Peng, R. Qin, S. Malola, B. K. Teo, H. Häkkinen and N. Zheng, *Angew. Chem., Int. Ed.*, 2021, **60**, 3752–3758.

113 K. Yamamoto, T. Imaoka, M. Tanabe and T. Kambe, *Chem. Rev.*, 2020, **120**, 1397–1437.

114 K. Yonesato, H. Ito, D. Yokogawa, K. Yamaguchi and K. Suzuki, *Angew. Chem., Int. Ed.*, 2020, **59**, 16361–16365.

115 K. Yonesato, H. Ito, H. Itakura, D. Yokogawa, T. Kikuchi, N. Mizuno, K. Yamaguchi and K. Suzuki, *J. Am. Chem. Soc.*, 2019, **141**, 19550–19554.

116 K. Yonesato, D. Yanai, S. Yamazoe, D. Yokogawa, T. Kikuchi, K. Yamaguchi and K. Suzuki, *Nat. Chem.*, 2023, **15**, 940–947.

117 K. Sakamoto, S. Masuda, S. Takano and T. Tsukuda, *ACS Catal.*, 2023, **13**, 3263–3271.